

## Article

# The Effect of Fiber End on the Bonding Mechanical Properties between SMA Fibers and ECC Matrix

Zhao Yang<sup>1,2,\*</sup> , Tingyu Deng<sup>1</sup> and Qingshi Fu<sup>1</sup>

<sup>1</sup> School of Urban Construction, Wuhan University of Science and Technology, Wuhan 430065, China; dengty0728@163.com (T.D.); 15571143686@163.com (Q.F.)

<sup>2</sup> Hubei Provincial Engineering Research Center of Urban Regeneration, Wuhan University of Science and Technology, Wuhan 430065, China

\* Correspondence: yzwh77@163.com

**Abstract:** In order to investigate the effect of fiber end on the bonding mechanical properties between shape memory alloy (SMA) fibers and Engineered Cementitious Composites (ECC), this study designed and fabricated five groups of specimens with variations in SMA fiber end shape, diameter and depth-to-diameter ratio. Direct tensile tests were conducted on these specimens under displacement control. The failure modes, stress–strain curves and various performance indicators were analyzed to evaluate the bonding mechanical properties and the effects of different factors. The results revealed that for straight-end SMA fibers, increasing the diameter and depth-to-diameter ratio both led to a decrease in bonding strength. On the other hand, the N-shaped end provided sufficient anchorage force for SMA fibers, resulting in a maximum pull-out stress of 926.3 MPa and a fiber strength utilization of over 78%. Increasing the fiber diameter enhanced the maximum pull-out stress and maximum anchorage stress for N-shaped-end SMA fibers but reduced the fiber strength utilization. These research findings provide a solid theoretical basis and data support for achieving a synergistic effect between SMA fibers and the ECC matrix.

**Keywords:** shape memory alloy fiber; engineering cementitious composites; fiber pullout behavior; interfacial bonding performance



**Citation:** Yang, Z.; Deng, T.; Fu, Q.

The Effect of Fiber End on the Bonding Mechanical Properties between SMA Fibers and ECC Matrix. *Buildings* **2023**, *13*, 2027. <https://doi.org/10.3390/buildings13082027>

Academic Editors: Bo-Tao Huang, Jing Yu and Hao-Liang Wu

Received: 28 June 2023

Revised: 31 July 2023

Accepted: 5 August 2023

Published: 9 August 2023



**Copyright:** © 2023 by the authors. Licensee MDPI, Basel, Switzerland. This article is an open access article distributed under the terms and conditions of the Creative Commons Attribution (CC BY) license (<https://creativecommons.org/licenses/by/4.0/>).

## 1. Introduction

With the continuous expansion of modern urban construction, economic losses caused by earthquakes are increasing. The traditional seismic design concept, which aims to ensure life safety and prevent collapse, is no longer able to meet society's seismic requirements. In order to enable structures to quickly regain their functionality and minimize economic losses after an earthquake, the concept of resilient seismic structures [1] has received widespread attention and been a focus of research in recent years. Various systems have been developed, including rocking structures, self-centering structures and replaceable component structures [2–4]. Among them, research at the material level to achieve functional recovery of structures has become a research hotspot.

Shape Memory Alloy (SMA), initially applied in precision and cutting-edge fields such as aerospace, robotics and medicine, has seen rapid development in research and application in civil engineering as material processing techniques and industrial production capabilities have advanced. SMA exhibits excellent superelasticity, generating recovery forces during loading–unloading cycles that facilitate crack closure and deformation recovery in structures [5]. Consequently, superelastic SMA is employed to enhance the self-centering and energy dissipation capabilities of structures, such as in the fabrication of dampers, supports and other energy dissipation and self-centering devices [6–8], or directly in strengthening structural components like shear walls and beams [9–11]. However, when SMA is applied to conventional concrete structures, the limited tensile deformation

capacity of concrete materials prevents the full utilization of the excellent performance of SMA materials.

Engineered Cementitious Composite (ECC) is a cement-based composite material reinforced with short fibers, known for its high strength, high ductility and strain-hardening behavior [12–14]. The ultimate tensile strain of ECC is 300 times higher compared to traditional cementitious materials. At the same time, the crack width of ECC is controlled to less than 100  $\mu\text{m}$ , which has excellent crack control capability [15]. ECC structures not only exhibit excellent collapse resistance but also possess high damage tolerance, resulting in significantly reduced residual crack widths after seismic events and consequently reducing post-earthquake maintenance costs [16,17]. When the appropriate fiber type and size are selected and the fiber/matrix interface is modified, ECC can achieve the required tensile strain capacity [18].

The combination of superelastic shape memory alloy (SMA) and Engineered Cementitious Composite (ECC) forms SMA-ECC composite material, which overcomes the drawbacks of concrete material's brittleness under tension and significant residual strain due to the yielding of steel reinforcement. The SMA-ECC composite exhibits advantages such as high ductility, strong energy dissipation capability and the ability to achieve crack closure and deformation recovery through the superelasticity of SMA [19,20]. It is particularly suitable for resilient seismic-resistant structures [21]. However, most current SMA materials are in the form of bars, rods, or wires, which face challenges in processing, requiring specialized fixtures or anchorage, and are prone to damage at connection points and high costs, limiting the widespread application of SMA materials. SMA fibers, on the other hand, offer advantages such as simple processing, no requirement for specialized anchorage and lower costs. Moreover, uniformly distributed SMA fibers are more suitable for ECC matrices with multiple cracks [22]. However, due to the smooth surface of the material, the bonding between SMA fibers and the matrix material is prone to interface debonding [23,24], leading to the underutilization of SMA's mechanical properties and material waste. Various methods have been explored by researchers to improve the bonding performance between SMA and the matrix material [25–28], achieving some results. However, overall, research on the bonding performance between SMA fibers and ECC is still scarce, and effective methods to enhance the bond strength between SMA fibers and ECC matrix are lacking. Strong bonding is essential to ensure the effective utilization of SMA fiber's material properties and is a primary issue to address in SMA-ECC composite material research.

Our previous research [29,30] has shown that the presence of fiber end anchorage can effectively enhance the bonding and anchorage strength between SMA fibers and ECC matrices. However, the previous studies employed knotted-end shapes, which are challenging to precisely control in terms of the end shape dimensions and involve difficult processing, limiting their suitability for large-scale production. Therefore, in this study, we fabricated SMA fibers with curved and N-shaped ends and investigated their bonding performance in ECC matrices. Through direct tensile tests on individual fibers, we analyzed the bonding failure modes, pull-out stress, shear strength, anchorage stress and fiber strength utilization, which are key mechanical properties. We compared the effects of SMA fiber end shapes, diameter and depth-to-diameter ratio (embedding depth/diameter) as influencing factors. These findings provide a basis for understanding the bonding performance between SMA fibers and ECC matrices, as well as for establishing relevant theoretical calculation models.

## 2. Materials and Methods

### 2.1. SMA Fibers

Direct tensile tests were conducted on nickel-titanium (NiTi) superelastic SMA fibers with diameters of 1.0 mm, 1.2 mm and 1.5 mm. The gauge length (measuring section length) was set at 100 mm. The stress–strain curves for the direct tensile testing of the SMA fibers are shown in Figure 1a, and the main performance parameters are presented

in Table 1. From Figure 1a, it can be observed that all three SMA fibers with different diameters exhibit distinct martensitic transformation plateaus. According to Table 1, as the diameter increases, the martensitic transformation stress and peak stress of the SMA fibers increase, and the ultimate tensile strain decreases.

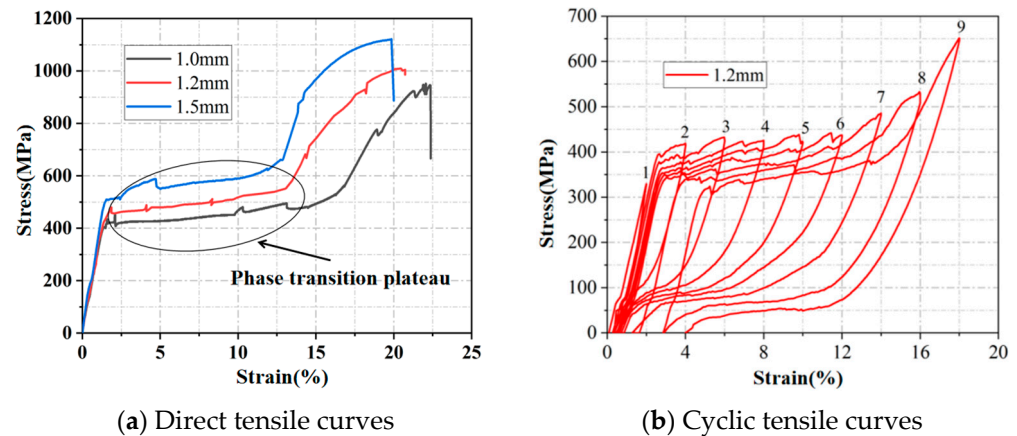


Figure 1. Tensile stress–strain curves of SMA fibers.

Table 1. The main performance parameters of SMA fibers.

Diameter (mm)	Elastic Modulus (GPa)	The Martensitic Phase Transition Begins/MPa		The Martensitic Phase Transition Ends/MPa		Peak Stress <sup>a</sup> (MPa)	Ultimate Strain <sup>b</sup> (%)
		Strain (%)	Stress (MPa)	Strain (%)	Stress (MPa)		
1.0	23.0	1.8	418.14	14.5	506.92	941.9	22.4
1.2	30.3	1.6	484.65	13.2	543.78	1001.1	21.8
1.5	34.0	1.5	509.89	12.9	652.51	1126.8	20.1

<sup>a</sup> The peak stress is defined as the maximum tensile stress obtained from the stress–strain curve of the SMA fiber under direct tensile loading. <sup>b</sup> The ultimate tensile strain refers to the maximum strain observed in the stress–strain curve of the SMA fiber under direct tensile loading.

To verify the superelastic behavior of the SMA fiber at room temperature, a cyclic tensile test was conducted on a 1.2 mm SMA fiber. The test employed displacement-controlled loading with a displacement increment of 2 mm per cycle. The stress–strain curve obtained from the test is shown in Figure 1b. From Figure 1b, it can be observed that the SMA fiber undergoes martensitic transformation starting from the second loading cycle and ending at the sixth cycle. In these cycles, the stress–strain curves of the SMA fiber exhibit a distinct flag-shaped characteristic, and the strain recovery rate within each cycle exceeds 98% [31]. Then, the fiber enters the hardening stage, and the recovery rate decreases gradually. By the ninth cycle with a strain of 18%, the strain recovery rate of this cycle still reaches 77%. These results indicate that the SMA fiber used in this experiment exhibits excellent superelastic performance at room temperature.

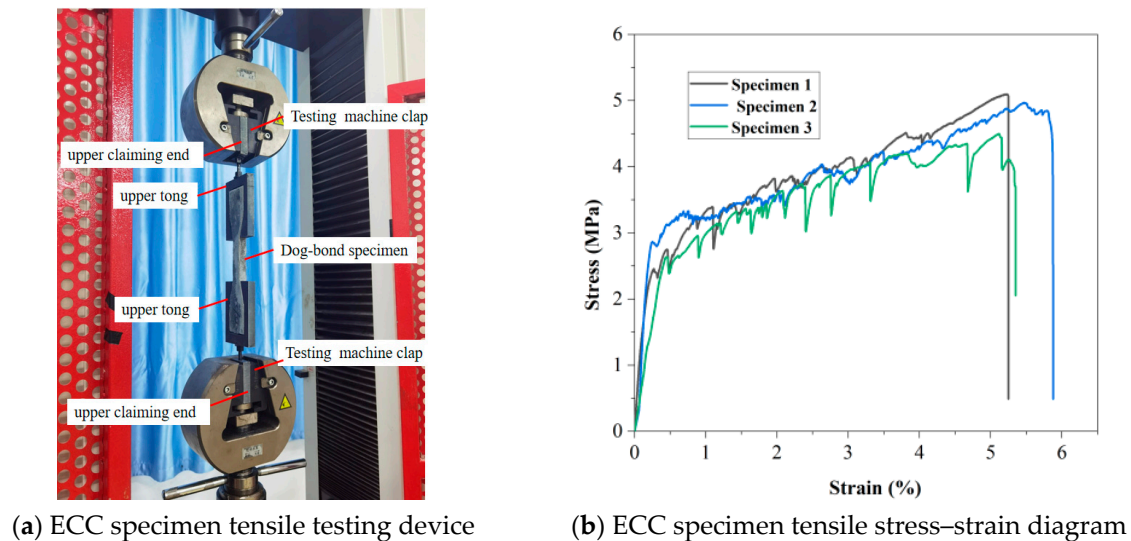
## 2.2. Engineered Cementitious Composite (ECC)

In order to improve the deformability of ECC material, based on reference [32] and through extensive trial mixes, the research group determined the mix proportions of ECC used in the experiments, as presented in Table 2. Following the specifications of JC/T 2461-2018 [33], three identical dog-bone-shaped ECC specimens were prepared using the mix proportions shown in Table 2. Tensile tests on the ECC specimens were conducted using the testing apparatus depicted in Figure 2a, yielding the tensile mechanical properties of the ECC material, as shown in Table 3. The stress–strain curve of the ECC specimens under tension is presented in Figure 2b. The average initial cracking strength of the ECC material was 2.59 MPa, with an elastic modulus of 9.5 GPa, a peak stress of 4.68 MPa and an ultimate tensile strain of 5.50%. These mechanical properties of ECC are comparable to those reported in the related literature [34].

**Table 2.** Mix proportions of ECC.

Raw Materials	Cement	Fly Ash	Sand	Water	Water Reducer	PVA (%) *
Mix proportion	1	4	0.2	0.22	0.0079	2

\* Percentage of fiber content by volume.

**Figure 2.** ECC tensile test device and result.**Table 3.** Tensile mechanical properties of ECC materials.

Number	Initial Crack Strength (MPa)	Initial Fission Strain (%)	Tensile Modulus of Elasticity (GPa)	Peak Stress (MPa)	Ultimate Tensile Strain (%)
1	2.43	0.27	9.0	5.12	5.24
2	2.74	0.19	11.3	4.78	5.95
3	2.59	0.32	8.1	4.33	5.32
The average	2.59	0.26	9.5	4.68	5.50

### 2.3. SMA-ECC Pull-Out Specimen Design

To investigate the influence of end shapes on the bonding mechanical properties between SMA fibers and the ECC matrix, direct pull-out tests were conducted in this experiment. Semi-dog-bone-shaped specimens consisting of SMA fibers and the ECC matrix were designed and prepared, as shown in Figure 3a. From top to bottom in Figure 3a, the specimens had a straight-end shape, curved-end shape and N-end shape, respectively. Here,  $L_e$  represents the embedded length of SMA fibers in the ECC matrix, and detailed dimensions are presented in Figure 3b. The mix proportions of the ECC matrix used in the specimens are provided in Table 2. During the specimen fabrication process, PVC plastic boards were placed in corresponding positions of the mold to form the semi-dog-bone-shaped mold, and the joints were sealed with hot-melt adhesive to prevent water leakage. Then, the prepared SMA fibers were threaded through the center of the PVC plastic boards and placed at designated positions according to the experimental grouping requirements. Finally, the ECC matrix was poured into the mold to fabricate the pull-out specimens. After the completion of specimen fabrication (Figure 4), the specimens were placed in a standard curing box for 48 h, followed by demolding and continued standard curing in a water tank for 28 days. It is worth mentioning that during the production of SMA fiber ends, high-temperature air guns were used to heat and soften the SMA fibers, which were then shaped into curved-end or N-end shapes before being cooled and hardened to achieve the desired end shapes. Furthermore, to ensure that the properties of the SMA material remained unchanged after heat treatment, the research group also conducted

tensile mechanical tests on the SMA fibers after the high-temperature heat treatment. The test results showed no significant differences in the mechanical properties between the heat-treated SMA fibers and the untreated SMA fibers, which is consistent with the findings of other researchers [35,36].

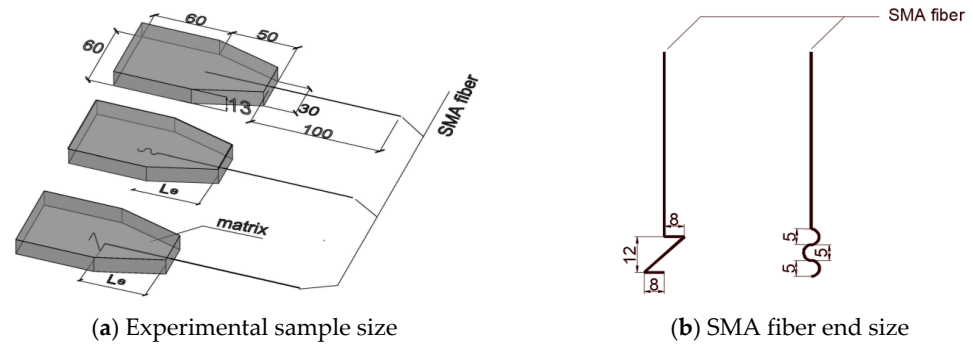


**Figure 3.** Specific size of the semi-dog-bone drawing specimen. (size unit in mm).

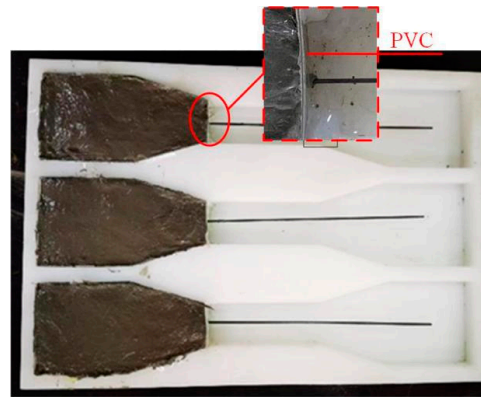


**Figure 4.** Pull-out specimen.

Three types of end shapes, namely, straight, curved and N-end, were selected for the SMA fibers. The diameters of the SMA fibers used were 1.0 mm, 1.2 mm and 1.5 mm, respectively. The bonding lengths between the SMA fibers and the ECC matrix were set at 30 mm, 33.3 mm, 40 mm, 50 mm and 60 mm (the lengths of curved- and N-ends were not included in the bonding length). The depth-to-diameter ratios (embedding length of SMA fibers in the matrix divided by the fiber diameter) were set at 25, 33.3, 41.7 and 50, respectively. To compare the effects of different parameters, five sets of pull-out specimens were designed, resulting in a total of 27 different types and three specimens for each type, amounting to a total of 51 specimens. The specific grouping of specimens is presented in Table 4.

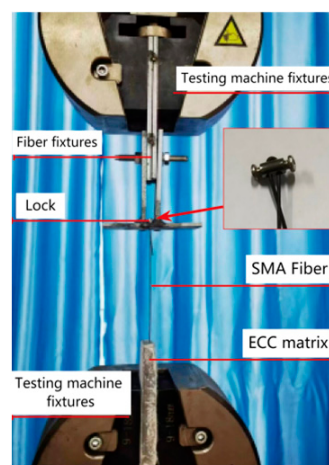
#### 2.4. Pull-Out Mechanical Properties

The pull-out test setup is illustrated in Figure 5, utilizing a universal testing machine (UTM) for uniaxial tension. Load application was controlled by displacement, with a loading rate of 1 mm/min. The initial length of the SMA fiber pull-out section was set to 100 mm. The UTM's built-in load and displacement sensors were employed to record the applied load and resulting displacements, respectively. The entire test process was controlled, and data were synchronized using a computer. The test was terminated when the SMA fiber was completely pulled out from the matrix, fractured or when the load value displayed by the testing machine became negative, indicating failure of the specimen. The ECC matrix portion of the pull-out specimen was fixed using a fixture located beneath the UTM. A specially designed fixture for the SMA fiber was employed, which involved threading the SMA fiber through a locking mechanism in the fixture and securing the

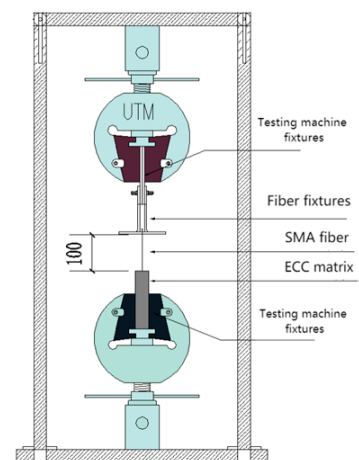
fiber fixture within another fixture located above the UTM. This setup prevented slippage between the SMA fiber and the testing machine fixture.

**Table 4.** Specimen grouping table.

Number	Number of Test Pieces	Specimen Number	End Shape	Depth-To-Diameter Ratio	Diameter/mm
1	3	S-33.3-1.0	Straight	33.3	1.0
	3	S-33.3-1.2		33.3	1.2
	3	S-33.3-1.5		33.3	1.5
2	3	S-25-1.2	Straight	25	1.2
	3	S-33.3-1.2		33.3	1.2
	3	S-41.7-1.2		41.7	1.2
	3	S-50-1.2		50	1.2
3	3	S-33.3-1.2	Straight	33.3	1.2
	3	C-33.3-1.2	Curved		
	3	N-33.3-1.2	N-end		
4	3	N-33.3-1.0	N-end	33.3	1.0
	3	N-33.3-1.2			1.2
	3	N-33.3-1.5			1.5
5	3	N-25-1.2	N-end	25	1.2
	3	N-33.3-1.2		33.3	
	3	N-41.7-1.2		41.7	
	3	N-50-1.2		50	



**(a)** Real-life photo



**(b)** Schematic diagram

**Figure 5.** Pictures of pulling device (size unit in mm).

### 3. Pull-Out Test Results

#### 3.1. Failure Mode

In this experiment, three failure modes were observed for the specimens, namely, pull-out failure, fracture failure and splitting failure, as shown in Figure 6. In the case of pull-out or fracture failure, no cracks were observed on the surface of the ECC and the matrix remained intact. However, in the case of splitting failure, significant cracking was observed on the ECC surface, indicating severe damage to the ECC matrix. The experimental results showed that the specimens with straight- and curved-end SMA fiber ends primarily experienced pull-out failure. For the specimens with straight-end SMA fiber ends, as the load increased, the bond strength between the SMA fiber and the ECC matrix gradually diminished, resulting in fiber debonding and sliding. Once the SMA

fiber completely debonded from the matrix, it was pulled out. In the case of specimens with curved SMA fiber ends, the curved shape provided some anchorage force as the linear portion of the fiber debonded and slid. However, due to stress concentration at the fiber end, the local mechanical anchorage force of the ECC matrix on the SMA fiber was insufficient, leading to the failure of anchorage and subsequent fiber sliding and pull-out. Therefore, the failure mode for these specimens was also pull-out. The specimens with N-shaped SMA fiber ends are mainly subjected to fiber breakage damage or, when the fiber depth diameter is relatively small, to matrix splitting damage. This indicates that the N-shaped end provided sufficient anchorage force for the SMA fiber, preventing premature failure by preventing the fiber from sliding out of the ECC matrix. This ensured that the stress in the SMA fiber could continue to increase, providing effective excitation for the superelasticity of the SMA.

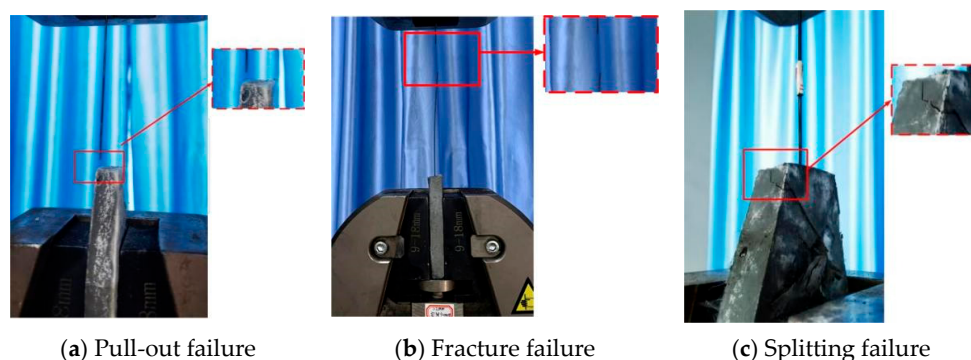


**Figure 6.** Test piece failure mode.

### 3.2. SMA Fiber Pull-Out Stress-Displacement Curve

The stress level experienced by the SMA fiber during the pull-out test is an important indicator for determining whether the SMA material can reach the stress plateau for phase transformation and effectively exhibit superelasticity. The experimental setup allows for the collection of load data by the computer system, and the pull-out stress of the SMA fiber can be calculated using Equation (1).

$$\sigma_f = \frac{P}{\pi \frac{d_f^2}{4}} \quad (1)$$

where,  $d_f$  is the diameter of the SMA fiber, and  $P$  is the SMA fiber loading end of the tensile load.

By utilizing Equation (1) to calculate the pull-out stress of the SMA fiber and its corresponding displacement at the loading end, the stress–displacement relationship curve of the SMA fiber during the pull-out test can be obtained. This curve provides an accurate understanding of the stress levels and development of the SMA fiber throughout the entire loading process. The stress–displacement curves of the specimens from different groups are compared in Figure 7, which reveals distinct stress development processes depending on the different shapes of SMA fiber ends.

From Figure 7a,b, it can be observed that the stress–displacement curves of SMA fibers with straight-end configuration can be divided into two stages: the elastic stage and the debonding stage. In the initial loading stage, the displacement at the loading end of the SMA fiber is relatively small, and the pull-out stress increases linearly with displacement until it reaches the peak stress, which corresponds to the elastic stage. As the displacement increases, the pull-out stress of the SMA fiber continues to decrease until it reaches zero, indicating the debonding stage between the fiber and the matrix. The peak stresses of these specimens' SMA fibers range from 251.3 MPa to 310.6 MPa, which do not reach the starting stress of the SMA phase transformation (Table 1). Therefore, the SMA fibers in these types of specimens do not exhibit superelastic behavior throughout the entire tensile process,

indicating insufficient anchorage provided by the straight-end configuration. Furthermore, from Figure 7a, it can be observed that as the diameter increases, the stress of the SMA fiber increases at a faster rate with displacement before reaching the peak stress. However, both the peak stress and maximum displacement decrease. This phenomenon can be attributed to the sliding stage of the fiber, where a larger diameter leads to a smaller relative bonding area and lower ultimate bonding strength. In the descending and residual stages, a larger diameter results in a faster decrease in average bonding stress and relatively less sliding [37]. From Figure 7b, it can be seen that within a certain range, as the depth-to-diameter ratio increases, the rate of stress increase with displacement before reaching the peak stress slows down, whereas both the peak stress and maximum displacement increase. This can be attributed to the increase in relative bonding area and the corresponding increase in ultimate bonding strength due to the larger depth-to-diameter ratio [38].

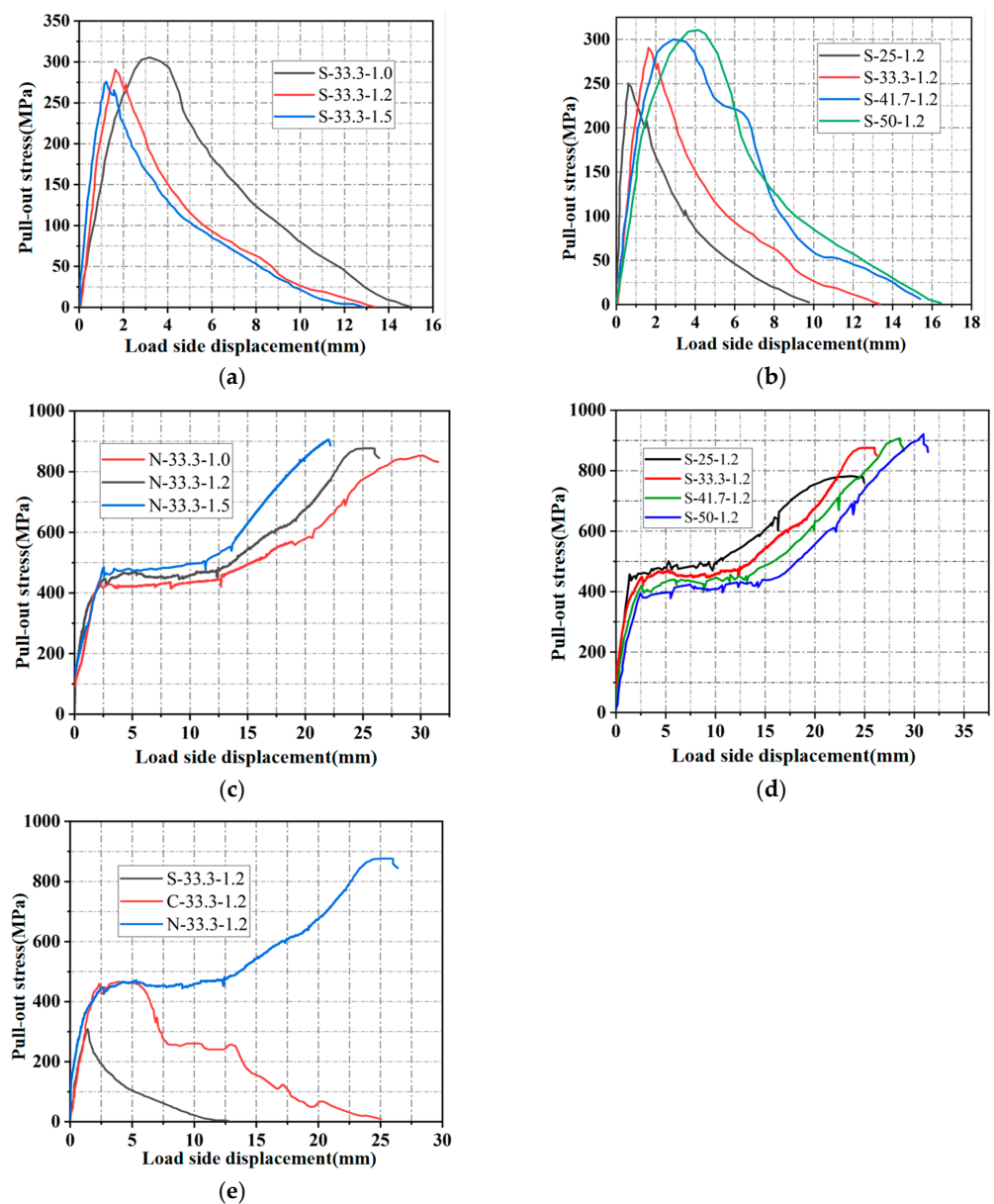


**Figure 7.** Pull-out stress–displacement curve of different groups of specimens. (a) Straight-end SMA fibers of different diameters; (b) Straight-end SMA fibers with different depth-to-diameter ratios; (c) N-shaped-end SMA fibers of different diameters; (d) N-shaped-end SMA fibers with different depth-to-diameter ratios; (e) SMA fibers with different end shapes.

From Figure 7c,d, it can be observed that the stress–displacement curves of SMA fibers with N-shaped ends can be divided into three stages: the elastic stage, the martensitic phase transformation stage and the martensitic hardening stage. In the initial loading stage, the specimens undergo an elastic stage similar to that of the SMA fibers with a straight-end configuration. As the displacement at the loading end of the SMA fiber increases, a stress plateau appears, which corresponds to the martensitic phase transformation stage. When the displacement at the loading end continues to increase, the pull-out stress of the SMA fiber significantly rises until failure, indicating the martensitic hardening stage. The peak stress of the SMA fiber in these specimens is 936.2 MPa, significantly exceeding the stress required for the SMA phase transformation. The SMA fiber undergoes a complete martensitic phase transformation and enters the martensitic hardening stage, effectively activating its superelastic behavior. From Figure 7c, it can be observed that as the diameter increases, the peak stress slightly increases. This can be attributed to the fact that the bonding strength of the N-shaped-end specimens mainly comes from the end anchorage. With a larger diameter, the fiber stiffness increases, leading to a greater mechanical anchorage force between the fiber and the matrix, resulting in higher pull-out stress [39]. From Figure 7d, it can be seen that with an increase in the depth-to-diameter ratio, the duration of the martensitic phase transformation stage slightly increases and the peak stress increases. This is because the increased effective bonding length brings higher frictional force, thereby enhancing the bonding strength of the specimens [40].

From Figure 7e, it can be observed that the SMA fibers with a curved end can reach the stress required for phase transformation. However, as the plastic deformation of the fiber at the curved end increases due to the phase transformation, the mechanical anchorage force between the curved end and the matrix decreases, leading to the failure of end anchorage. Consequently, the fiber is unable to complete the phase transformation and enter the martensitic hardening stage. On the other hand, the straight-end fibers cannot undergo the SMA phase transformation, whereas the N-shaped-end fibers can enter the martensitic hardening stage, which is consistent with the phenomena described earlier.

#### 4. The Bonding Mechanical Property Indexes and Influencing Factors

##### 4.1. Calculation of the Bonding Mechanical Property Indexes

##### 4.1.1. SMA Strength Utilization

The bonding force between SMA fibers and the ECC matrix includes the interfacial shear force  $V$  (comprising adhesive force and frictional force) and the end anchorage force. The pull-out load  $P$  is equal to the sum of the interfacial shear force and the end anchorage force, as shown in Equation (2). The force diagram is illustrated in Figure 8.

$$P = V + F_a \quad (2)$$

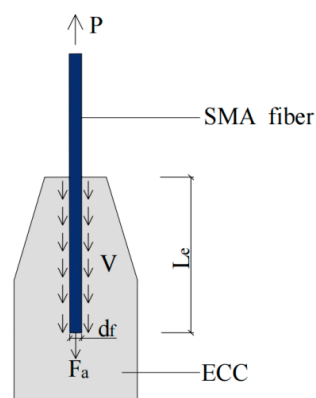


Figure 8. Pull-out force diagram.

For SMA fibers with a straight end, the bonding force is solely the interfacial shear force  $V$ . Therefore, the average interfacial shear stress  $\tau_{\max}$  can be calculated using Equation (3).

$$\bar{\tau} = \frac{P}{\pi d_f L_e} \quad (3)$$

where  $d_f$  represents the diameter of the SMA fiber, and  $L_e$  represents the length of the SMA fiber embedded in the matrix. When the load reaches its maximum value  $P_{\max}$ , the corresponding average shear stress  $\bar{\tau}_{\max}$  is regarded as the average shear strength.

#### 4.1.2. Anchorage Stress

For SMA fibers with non-straight ends (curved and N ends), the bonding force includes both interface shear force  $V$  and end anchorage force  $F_a$ . The end anchorage force  $F_a$  can be approximately calculated as the increase in bonding force for non-straight-end fibers compared to straight-end fibers under same conditions, such as the same fiber diameter and same embedding length, as shown in Equation (4). The pull-out stress of the SMA fiber resulting from the end anchorage force is called anchorage stress  $f_a$ , which can be calculated using Equation (5).

$$F_a = P_{\max}^E - P_{\max} \quad (4)$$

$$f_a = \frac{4(P_{\max}^E - P_{\max})}{\pi d_f^2} \quad (5)$$

where  $P_{\max}^E$  is the maximum pull-out load of the specimen with a non-straight-end SMA fiber, and  $P_{\max}$  is that of the specimen with a straight-end SMA fiber under the same condition.

#### 4.1.3. SMA Strength Utilization

In order to assess the utilization of material strength in SMA fibers, the fiber strength utilization ratio  $u_f$  is introduced, which is the ratio of the maximum pull-out stress in the fiber to its tensile strength, as shown in Equation (6).

$$u_f = (\sigma_{f,\max} / f_y) \cdot 100\% \quad (6)$$

where  $\sigma_{f,\max}$  is the maximum pull-out stress of the SMA fiber, and  $f_y$  is the ultimate tensile strength of the SMA fiber.

The improvement in fiber strength utilization due to the fiber end anchorage is represented by the fiber utilization rate difference  $\Delta u_f$ , as shown in Equation (7).

$$\Delta u_f = (f_a / f_y) \cdot 100\% \quad (7)$$

#### 4.1.4. Calculation Results of the Bonding Mechanical Property Indexes

Based on the tensile strength of SMA fiber (Table 1) and Equations (2) to (7), the bonding mechanical property indexes of SMA fiber in the pull-out test at the ultimate state can be calculated. The calculation results are presented in Table 5.

**Table 5.** SMA fiber bonding academic performance index.

Group	Specimen Number	$P_{\max}/N$	$\bar{\tau}/MPa$	$f_y/MPa$	$\sigma_{f,\max}/MPa$	$f_a/MPa$	$u_f/\%$	$\Delta u_f/\%$	Failure Mode
1	S-33.3-1.0	241.2	2.3	941.9	307.2	----	32.6	----	Pull-out failure
	S-33.3-1.2	328.4	2.2	1001.1	290.5	----	29.0	----	Pull-out failure
	S-33.3-1.5	486.4	2.1	1120.4	275.4	----	24.6	----	Pull-out failure

Table 5. Cont.

Group	Specimen Number	$P_{\max}/N$	$\bar{\tau}/MPa$	$f_y/MPa$	$\sigma_{f,\max}/MPa$	$f_a/MPa$	$u_f/\%$	$\Delta u_f/\%$	Failure Mode
2	S-25-1.2	284.1	2.5	1001.1	251.3	----	25.1	----	Pull-out failure
	S-33.3-1.2	328.4	2.2	1001.1	290.5	----	29.0	----	Pull-out failure
	S-41.7-1.2	339.3	1.8	1001.1	300.2	----	30.0	----	Pull-out failure
	S-50-1.2	351.1	1.6	1001.1	310.6	----	31.0	----	Pull-out failure
3	S-33.3-1.2	328.4	2.2	1001.1	290.5	----	29.0	----	Pull-out failure
	C-33.3-1.2	525.7	----	1001.1	465.1	174.6	46.5	17.4	Pull-out failure
	N-33.3-1.2	990.1	----	1001.1	875.9	585.4	87.5	58.5	Fracture failure
4	N-33.3-1.0	668.1	----	941.9	851.1	543.9	90.4	57.7	Fracture failure
	N-33.3-1.2	990.1	----	1001.1	875.9	585.4	87.5	58.5	Fracture failure
	N-33.3-1.5	1598.6	----	1120.4	905.1	629.7	80.8	56.2	Splitting failure
	N-25-1.2	884.0	----	1001.1	782.2	491.7	78.1	49.1	Splitting failure
	N-33.3-1.2	990.1	----	1001.1	875.9	585.4	87.5	58.5	Fracture failure
	N-41.7-1.2	1025.2	----	1001.1	906.9	616.4	90.6	61.6	Fracture failure
	N-50-1.2	1047.1	----	1001.1	926.3	615.7	92.5	61.5	Fracture failure

## 4.2. Influencing Factors of Bonding Mechanical Property Indexes

### 4.2.1. Straight-End SMA Fiber

#### (1) Effect of diameter on the bonding mechanical properties

To investigate the influence of different diameters of straight-end SMA fibers on bonding mechanical property indexes, three groups of specimens with different diameters, namely, S-33.3-1.0, S-33.3-1.2 and S-33.3-1.5, were selected for comparison.

According to Table 5 and Figure 9a, the peak stresses of the mentioned specimens are 307.2 MPa, 290.5 MPa and 275.4 MPa, with fiber strength utilizations of 32.6%, 29% and 24.6%, respectively. This indicates that as the diameter increases, both the peak stress and fiber strength utilization of the SMA fiber gradually decrease. This phenomenon can be attributed to the Poisson effect that occurs in SMA fibers under stress. As the fiber diameter increases, the transverse contraction strain also increases, resulting in a faster reduction in frictional force between the SMA fiber and the matrix, accelerating the failure of chemical bonding strength. Consequently, the peak stress of the SMA fiber decreases with increasing diameter [41]. Additionally, according to Table 1, the tensile strength of the SMA fiber increases with diameter. As a result, based on Equation (6), the pull-out stress is directly proportional to the fiber strength utilization, therefore, when the peak pull-out stress of the fiber decreases, the fiber strength utilization decreases.

According to Table 5 and Figure 9b, the average shear strengths are 2.3 MPa, 2.2 MPa and 2.1 MPa for the respective specimens. Based on the analysis of peak stress mentioned above, as the diameter increases, the transverse contraction strain also increases, so the Poisson effect causes a decrease in both the frictional force and bonding strength between the SMA fiber and the matrix. Consequently, this leads to a reduction in shear strength.

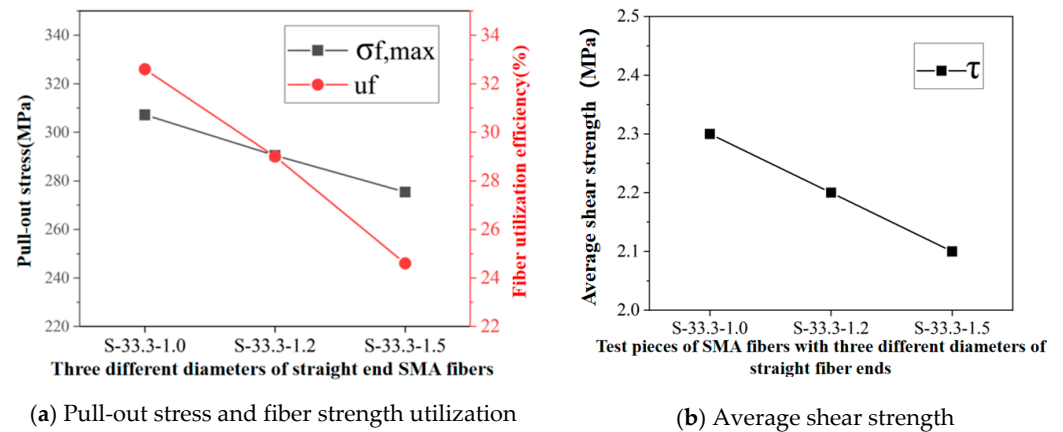
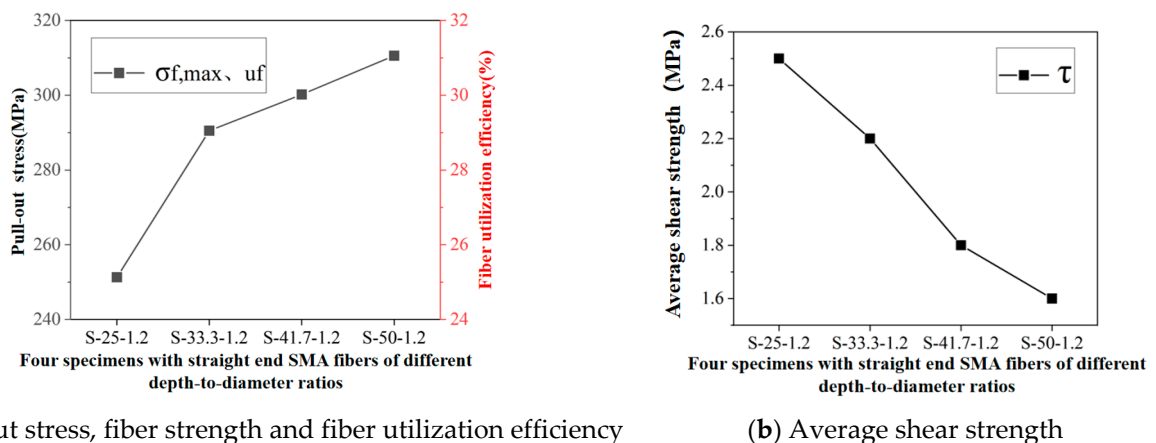


Figure 9. Effect of different diameters on the bonding properties of straight-end SMA fibers.

(2) Effect of depth-to-diameter ratio on the bonding mechanical properties

To investigate the influence of different depth-to-diameter ratios on the bonding mechanical properties of straight-end SMA fibers, four sets of specimens with varying depth-to-diameter ratios, namely, S-25-1.2, S-33.3-1.2, S-41.7-1.2 and S-50-1.2, were selected for comparison.

According to Table 5 and Figure 10a, the peak stresses of the aforementioned specimens are 251.3 MPa, 290.5 MPa, 300.2 MPa and 310.6 MPa, with fiber strength utilization ratios of 25.1%, 29.0%, 30.0% and 31.0%, respectively. This indicates that as the depth-to-diameter ratio increases, both the peak stress and fiber strength utilization ratio also increase. This can be attributed to the fact that for SMA fibers with the same diameter, as the embedment depth in the matrix increases, the contact area between the SMA fiber and the matrix increases. Consequently, the available bonding forces, including both interfacial adhesion and frictional forces, increase, leading to an increase in peak stress. Additionally, because the ultimate tensile strength of the SMA fiber remains constant for fibers with the same diameter, according to Equation (6), the fiber strength utilization ratio increases with the increase in peak stress.



(a) Pull-out stress, fiber strength and fiber utilization efficiency

(b) Average shear strength

Figure 10. Effect of different depth-to-diameter ratio on the bonding properties of straight-end SMA fibers.

According to Table 5 and Figure 10b, the average shear strengths of the aforementioned specimens are 2.5 MPa, 2.2 MPa, 1.8 MPa and 1.6 MPa, respectively. This indicates that as the depth-to-diameter ratio increases, the shear strength between the interfaces of the specimens decreases. This phenomenon can be attributed to the stress arching effect within the specimens, resulting in an uneven distribution of shear stress and the formation of stress

concentration peaks. As the depth-to-diameter ratio increases, i.e., when the embedment depth of the SMA fiber increases, the proportion of the effective stress region decreases. Consequently, the concentration of stress at the interface decreases, leading to a reduction in interfacial shear strength [42].

#### 4.2.2. Non-Straight-End SMA Fiber

##### (1) Effect of end shape on the bonding mechanical properties

In order to investigate the influence of different end configurations of SMA fibers on bonding mechanical properties, three groups of specimens with different end configurations, namely, S-33.3-1.2, C-33.3-1.2 and N-33.3-1.2, were selected for comparison.

From Figure 11a and Table 5, it can be observed that the peak stress values for the straight-, curved- and N-shaped-end specimens of SMA fibers are 290.5 MPa, 465.1 MPa and 875.9 MPa, respectively. The anchorage stress values for the curved- and N-shaped-end specimens are 174.6 MPa and 585.4 MPa, respectively. The failure mode for the straight- and curved-end specimens is pull-out failure, whereas the failure mode for the N-shaped-end specimens is fracture failure. The peak stress of the N-shaped-end specimens is 1.9 times higher than that of the curved-end specimens and 3.0 times higher than that of the straight-end specimens, indicating that the N-shaped end significantly improves the bonding strength between SMA fibers and the ECC matrix.

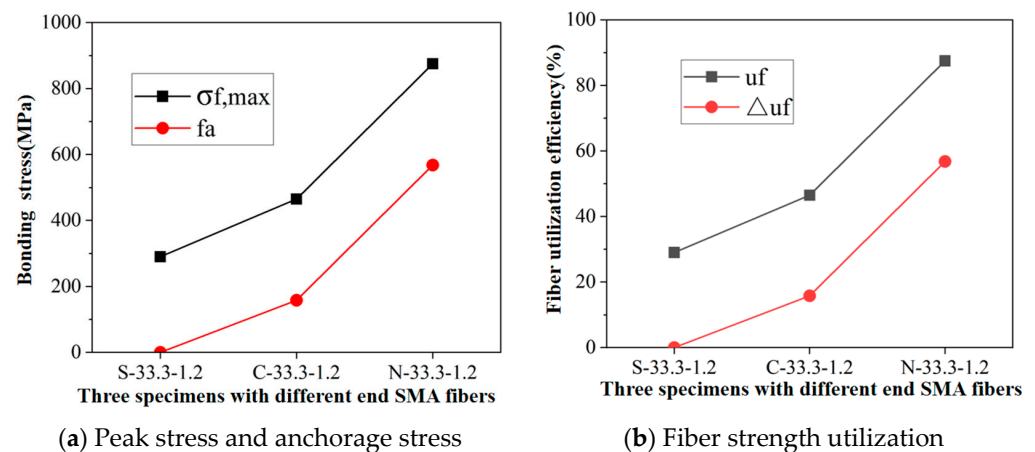


**Figure 11.** Effect of different end shapes on the bonding properties between SMA fibers and ECC matrix.

This can be attributed to the fact that the bonding performance of the straight-end specimens is limited because they rely solely on interfacial shear force to resist pull-out loads. Although the curved-end specimens can provide some anchorage force, stress concentration and deformation at the end of the fiber occur during the anchorage process, leading to a continuous reduction in mechanical interlocking force and premature anchorage failure [43]. On the other hand, the N-shaped end exhibits prominent mechanical interlocking, which can provide sufficient anchorage force. Hence, the peak stress of the N-shaped-end specimens is significantly higher than that of the straight- and curved-end specimens.

According to Table 5, the fiber strength utilization rate of the N-shaped-end specimens is increased by 58.5% compared to the straight-end specimens. This indicates that the anchorage force of the N-shaped end can significantly enhance the fiber strength utilization rate of SMA fibers, surpassing that of the curved- and straight-end specimens, which is consistent with the stress analysis conclusion presented above.

##### (2) Effect of fiber diameter on the bonding mechanical properties

To investigate the influence of fiber diameter on the bonding mechanical properties of N-shaped-end SMA fibers, three groups of specimens with different diameters, N-33.3-1.0, N-33.3-1.2 and N-33.3-1.5, were selected for comparison.

According to Table 5, the failure mode of SMA fibers with diameters of 1.0 mm and 1.2 mm is pull-out failure, whereas the failure mode of the fiber with a diameter of 1.5 mm is splitting failure. This phenomenon indicates that as the diameter of the SMA fiber increases, the mechanical anchorage force provided by the end becomes greater. When the anchorage force at the fiber end exceeds the shear carrying capacity of the matrix, insufficient shear resistance of the matrix occurs as the pull-out load increases, leading to splitting failure in the specimen [44]. This observation further confirms the excellent mechanical interlocking effect of the N-shaped end.

Moreover, as shown in Figure 12a, the anchorage stress of N-shaped-end specimens with diameters of 1.0 mm, 1.2 mm and 1.5 mm are 543.9 MPa, 585.4 MPa and 629.7 MPa, respectively. This indicates that the anchorage stress of the N-shaped end increases approximately linearly with the diameter. This phenomenon can be attributed to the fact that, under the condition of sufficient anchorage at the end, the resistance to pull-out of N-shaped-end SMA fibers mainly relies on the anchorage force at the end. As the diameter of the SMA fiber increases, the fiber's tensile strength and stiffness increase, resulting in greater mechanical anchorage force. Therefore, larger SMA fiber diameters result in higher anchorage stresses.

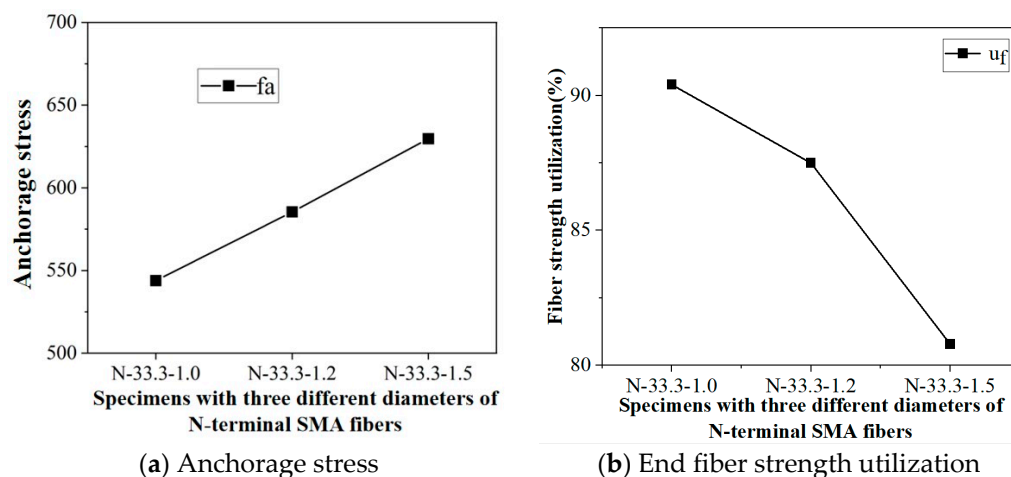


**Figure 12.** Effect of different diameters of N-shaped-end fibers on the bonding properties between SMA fibers and ECC matrix.

The fiber utilization rates of the N-shaped-end specimens with the three different diameters increased by 90.4%, 87.5% and 80.8%, respectively. Considering the occurrence of split failure in the 1.5 mm SMA fiber, it can be inferred that the decrease in fiber utilization rate is mainly attributed to the limited strength of the matrix, which cannot withstand the decreasing capacity to withstand the anchorage stress at the fiber end. This observation aligns with the conclusion reported in reference [45].

### (3) Effect of depth-to-diameter ratio on the bonding mechanical properties

To investigate the influence of the depth-to-diameter ratio on the bond mechanical properties of N-shaped-end SMA fibers, four sets of specimens with different depth-to-diameter ratios, namely, N-25-1.2, N-33.3-1.2, N-41.7-1.2 and N-50-1.2, were selected for comparison.

According to Table 5, the SMA fiber with a depth-to-diameter ratio of 25 exhibited a splitting failure mode, indicating insufficient embedding length of the SMA fiber within the matrix. However, as the depth-to-diameter ratio increased, all specimens experienced a fracture failure mode, indicating that the embedding length of the SMA fiber in the matrix was sufficient to achieve adequate anchorage at the ends.

Furthermore, as shown in Figure 13a, the aforementioned specimens exhibited anchorage stresses of 491.7 MPa, 585.4 MPa, 616.4 MPa and 615.7 MPa, respectively. This indicates that with an increase in the depth-to-diameter ratio, the anchorage stress initially rises and

then stabilizes. This behavior can be attributed to the fact that, under conditions where the fiber end is sufficiently anchored and the matrix has adequate shear resistance, the load-carrying capacity of the N-shaped-end SMA fiber primarily relies on the anchorage force at the end, but the depth of fiber embedding in the matrix has a relatively minor effect [46].

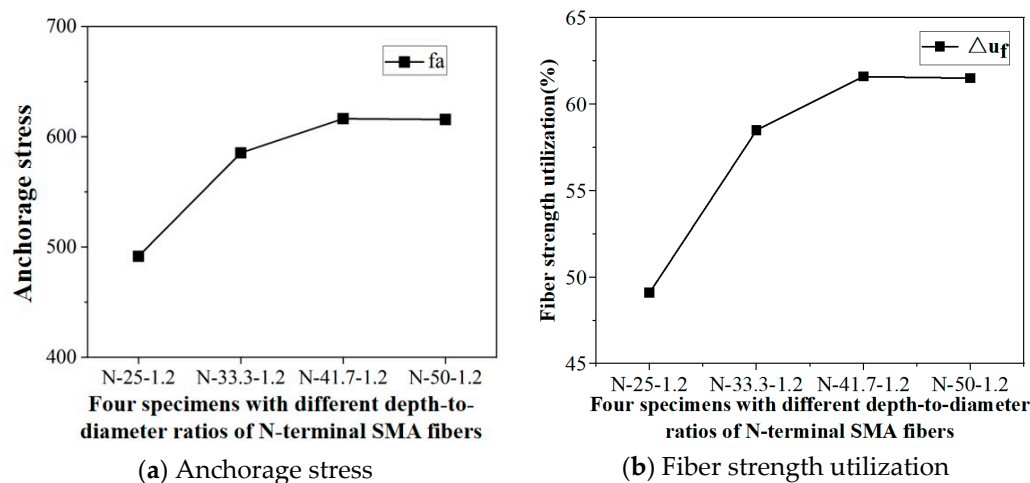


**Figure 13.** Effect of different depth-to-diameter ratio on the bonding properties between SMA fibers and ECC matrix.

The fiber utilization ratios of N-shaped-end SMA fibers with different depth-to-diameter ratios increased by 49.1%, 58.5%, 61.6% and 61.5%, respectively. This also indicates that, under conditions of sufficient fiber anchorage at the end and adequate shear resistance of the matrix, the depth of fiber embedding has a minor effect on the fiber utilization ratio.

## 5. Conclusions

To investigate the effect of fiber end on the bonding mechanical properties between SMA fibers and the ECC matrix, direct pull-out tests were conducted in this study. Parameters such as pull-out stress, average shear strength, anchorage stress and fiber utilization ratio were analyzed. The effects of SMA fiber end shape, diameter, and depth-to-diameter ratio were compared. The main research findings are summarized as follows:

1. The shear strength at the interface decreases as the depth-to-diameter ratio or diameter increases for SMA fibers with a straight end. The peak stress of SMA fibers with a straight end is 310.6 MPa, which is significantly lower than the stress level required for the martensitic transformation of SMA fibers. Consequently, the fibers do not undergo superelastic behavior, resulting in a low fiber utilization ratio.
2. Compared to the straight-end fibers, the peak stress of SMA fibers with a curved end is higher, at 465.1 MPa, which can reach the stress level required for martensitic transformation. However, during the anchorage process, the stress concentration and deformation at the curved end leads to a continuous reduction in mechanical interlocking force and premature anchorage failure, thereby preventing the full development of superelasticity.
3. The N-shaped end provides sufficient anchorage capacity for SMA fibers, significantly enhancing the bond strength between SMA fibers and the ECC matrix. The peak stress of SMA fibers can reach 875.9 MPa, which is 1.9 times and 3.0 times higher than that of curved-end and straight-end SMA fibers, respectively. This enables the stress in SMA fibers to reach the martensitic hardening stage until fiber fracture, thereby providing ample support for the full utilization of superelasticity in SMA fibers embedded in the ECC matrix.
4. Under the full anchorage condition, as the fiber diameter increases, the anchorage stress at the N-shaped end increases and the enhanced fiber strength utilization de-

creases. With an increase in the depth-to-diameter ratio, both the anchorage stress and the enhanced fiber strength utilization initially increase and then stabilize. When the depth-to-diameter ratio is 41.7, the anchorage stress and the enhanced fiber strength utilization reach their maximum values, namely, 616.4 MPa and 61.6%, respectively.

This study focused solely on experimental research, and further investigations are needed to explore relevant bonding mechanics models. Additionally, in future research, exploring the combination of surface treatments of SMA fibers and the implementation of end anchorage techniques could potentially enhance the bonding strength between SMA fibers and the ECC matrix.

**Author Contributions:** Conceptualization, Z.Y.; methodology, Z.Y.; formal analysis, T.D. and Q.F.; investigation, T.D. and Q.F.; data curation, T.D. and Q.F.; writing—original draft preparation, T.D.; writing—review and editing, Z.Y.; supervision, Z.Y.; project administration, Z.Y.; funding acquisition, Z.Y. All authors have read and agreed to the published version of the manuscript.

**Funding:** This research was funded by The National Natural Science Foundation of China, grant number 52178158, the Excellent Young and Middle-aged Science and Technology Innovation Team Plan of Hubei Provincial Department of Education, grant number Zy2022e004 and the Science and Technology Plan Project of Department of Housing and Urban-Rural Development of Hubei Province, grant number (2022)2198-76.

**Data Availability Statement:** Not applicable.

**Conflicts of Interest:** The authors declare no conflict of interest.

## References

1. Grigorian, M.; Moghadam, A.S.; Mohammadi, H.; Kamizi, M. Methodology for developing earthquake-resilient structures. *Struct. Des. Tall Spec. Build.* **2019**, *28*, e1571. [[CrossRef](#)]
2. Jia, M.; Gao, S.; Fu, F.; Yang, N. Failure mechanism and seismic performance evaluation of steel frame using rocking truss. *Structures* **2021**, *33*, 1180–1192. [[CrossRef](#)]
3. You, T.; Wang, W.; Tesfamariam, S. Effects of self-centering structural systems on regional seismic resilience. *Eng. Struct.* **2023**, *274*, 115125. [[CrossRef](#)]
4. Hu, H.; Liu, J.; Cheng, G.; Li, J.; Chen, Y.F. Seismic behavior of hybrid coupled wall system with replaceable endplate-steel coupling beam. *J. Constr. Steel Res.* **2021**, *187*, 106997. [[CrossRef](#)]
5. Abavisani, I.; Rezaifar, O.; Kheyroddin, A. Multifunctional properties of shape memory materials in civil engineering applications: A state-of-the-art review. *J. Build. Eng.* **2021**, *44*, 102657. [[CrossRef](#)]
6. Qian, H.; Fan, C.; Shi, Y.; Xu, J.; Li, Z.; Deng, E. Development and investigation of an innovative shape memory alloy cable-controlled self-centering viscoelastic coupling beam damper for seismic mitigation in coupled shear wall structures. *Earthq. Eng. Struct. Dyn.* **2023**, *52*, 370–393. [[CrossRef](#)]
7. Jiang, Z.-Q.; Chen, M.-L.; Yang, Z.-S.; Li, X.-Y.; Cai, C. Cyclic loading tests of self-centering prestressed prefabricated steel beam-column joint with weakened FCP. *Eng. Struct.* **2022**, *252*, 113578. [[CrossRef](#)]
8. Zhan, M.; Zhang, L.; Chen, X.; Wang, S.; Ma, Y. Experiment and Finite-Element Analysis on Seismic Response of Y-Shaped Porcelain Column Circuit Breaker Equipped with SMA Cables. *Int. J. Civ. Eng.* **2022**, *20*, 1211–1227. [[CrossRef](#)]
9. Qiang, X.; Chen, L.; Jiang, X. Achievements and Perspectives on Fe-Based Shape Memory Alloys for Rehabilitation of Reinforced Concrete Bridges: An Overview. *Materials* **2022**, *15*, 8089. [[CrossRef](#)]
10. Cortés-Puentes, W.L.; Palermo, D. SMA tension brace for retrofitting concrete shear walls. *Eng. Struct.* **2017**, *140*, 177–188. [[CrossRef](#)]
11. Cortés-Puentes, L.; Zaidi, M.; Palermo, D.; Dragomirescu, E. Cyclic loading testing of repaired SMA and steel reinforced concrete shear walls. *Eng. Struct.* **2018**, *168*, 128–141. [[CrossRef](#)]
12. Fakharifar, M.; Dalvand, A.; Arezoumandi, M.; Sharbatdar, M.K.; Chen, G.; Kheyroddin, A. Mechanical properties of high performance fiber reinforced cementitious composites. *Constr. Build. Mater.* **2014**, *71*, 510–520. [[CrossRef](#)]
13. Ding, Y.; Yu, K.; Li, M. A review on high-strength engineered cementitious composites (HS-ECC): Design, mechanical property and structural application. *Structures* **2022**, *35*, 903–921. [[CrossRef](#)]
14. Zhu, J.-X.; Xu, L.-Y.; Huang, B.-T.; Weng, K.-F.; Dai, J.-G. Recent developments in Engineered/Strain-Hardening Cementitious Composites (ECC/SHCC) with high and ultra-high strength. *Constr. Build. Mater.* **2022**, *342*, 127956. [[CrossRef](#)]
15. Zhang, M.; Zhu, X.; Liu, B.; Shi, J.; Gencel, O.; Ozbakkaloglu, T. Mechanical property and durability of engineered cementitious composites (ECC) with nano-material and superabsorbent polymers. *Powder Technol.* **2022**, *409*, 117839. [[CrossRef](#)]
16. Li, V.C. Applications of Engineered Cementitious Composites (ECC). In *Engineered Cementitious Composites (ECC): Bendable Concrete for Sustainable and Resilient Infrastructure*; Li, V.C., Ed.; Springer: Berlin/Heidelberg, Germany, 2019; pp. 313–369.

17. Suryanto, B.; Tambusay, A.; Suprobo, P.; Bregoli, G.; Aitken, M. Seismic performance of exterior beam-column joints constructed with engineered cementitious composite: Comparison with ordinary and steel fibre reinforced concrete. *Eng. Struct.* **2022**, *250*, 113377. [[CrossRef](#)]
18. Li, J.; Qiu, J.; Weng, J.; Yang, E.-H. Micromechanics of engineered cementitious composites (ECC): A critical review and new insights. *Constr. Build. Mater.* **2023**, *362*, 129765. [[CrossRef](#)]
19. Yucel, H.E.; Dutkiewicz, M.; Yildizhan, F. Application of ECC as a Repair/Retrofit and Pavement/Bridge Deck Material for Sustainable Structures: A Review. *Materials* **2022**, *15*, 8752. [[CrossRef](#)]
20. Qian, H.; Li, Z.; Pei, J.; Kang, L.; Li, H. Seismic performance of self-centering beam-column joints reinforced with superelastic shape memory alloy bars and engineering cementitious composites materials. *Compos. Struct.* **2022**, *294*, 115782. [[CrossRef](#)]
21. Qian, H.; Ye, Y.; Yan, C.; Jin, G.; Li, C.; Shi, Y. Experimental study on the seismic performance of self-centering bridge piers incorporating ECC and superelastic SMA bars in the plastic hinge regions. *Structures* **2022**, *46*, 1955–1967. [[CrossRef](#)]
22. Ali, M.A.E.M.; Soliman, A.M.; Nehdi, M.L. Hybrid-fiber reinforced engineered cementitious composite under tensile and impact loading. *Mater. Des.* **2017**, *117*, 139–149. [[CrossRef](#)]
23. Lei, H.; Wang, Z.; Tong, L.; Zhou, B.; Fu, J. Experimental and numerical investigation on the macroscopic mechanical behavior of shape memory alloy hybrid composite with weak interface. *Compos. Struct.* **2013**, *101*, 301–312. [[CrossRef](#)]
24. Shi, M.; Zhao, J.; Liu, J.; Wang, H.; Wang, Z.; Xu, L.; Sun, X. The Interface Adhesive Properties and Mechanical Properties of Shape Memory Alloy Composites. *Fibers Polym.* **2022**, *23*, 273–281. [[CrossRef](#)]
25. Lau, K.-T.; Tam, W.-Y.; Meng, X.-L.; Zhou, L.-M. Morphological study on twisted NiTi wires for smart composite systems. *Mater. Lett.* **2002**, *57*, 364–368. [[CrossRef](#)]
26. Smith, N.; Antoun, G.; Ellis, A.; Crone, W. Improved adhesion between nickel–titanium shape memory alloy and a polymer matrix via silane coupling agents. *Compos. Part A Appl. Sci. Manuf.* **2004**, *35*, 1307–1312. [[CrossRef](#)]
27. Yuan, G.; Bai, Y.; Jia, Z.; Hui, D.; Lau, K.-T. Enhancement of interfacial bonding strength of SMA smart composites by using mechanical indented method. *Compos. Part B Eng.* **2016**, *106*, 99–106. [[CrossRef](#)]
28. Choi, E.; Kim, D.; Lee, J.-H.; Ryu, G.-S. Monotonic and hysteretic pullout behavior of superelastic SMA fibers with different anchorages. *Compos. Part B Eng.* **2017**, *108*, 232–242. [[CrossRef](#)]
29. Yang, Z.; Du, Y.; Liang, Y.; Ke, X. Mechanical Behavior of Shape Memory Alloy Fibers Embedded in Engineered Cementitious Composite Matrix under Cyclic Pullout Loads. *Materials* **2022**, *15*, 4531. [[CrossRef](#)]
30. Yang, Z.; Gong, X.; Wu, Q.; Fan, L. Bonding Mechanical Properties between SMA Fiber and ECC Matrix under Direct Pullout Loads. *Materials* **2023**, *16*, 2672. [[CrossRef](#)]
31. Zhou, X.; Ma, B.; Wei, K.; Wang, X. Deformation recovery properties of asphalt mixtures with shape memory epoxy resin. *Constr. Build. Mater.* **2021**, *268*, 121193. [[CrossRef](#)]
32. Li, V.C.; Wang, S.; Wu, C. Tensile Strain-Hardening Behavior of Polyvinyl Alcohol Engineered Cementitious Composite (PVA-ECC). *ACI Mater. J.* **2001**, *98*, 483–492.
33. *JC/T 2461-2018*; Standard Test Method for the Mechanical Properties of Ductile Fiber Reinforced Cementitious Composites. Ministry of Industry and Information Technology of People’s Republic of China: Beijing, China, 2018.
34. Weimann, M.B.; Li, V.C. Hygral Behavior of Engineered Cementitious Composites (ECC)/Vergleich der hygri-schen Eigenschaften von ECC mit Beton. *Restor. Build. Monum.* **2003**, *9*, 513–534. [[CrossRef](#)]
35. Atli, K.; Karaman, I.; Noebe, R.; Garg, A.; Chumlyakov, Y.; Kireeva, I. Shape memory characteristics of Ti49.5Ni25Pd25Sc0.5 high-temperature shape memory alloy after severe plastic deformation. *Acta Mater.* **2011**, *59*, 4747–4760. [[CrossRef](#)]
36. Kim, H.Y.; Jinguu, T.; Nam, T.H.; Miyazaki, S. Cold workability and shape memory properties of novel Ti-Ni-Hf-Nb high-temperature shape memory alloys. *Scr. Mater.* **2011**, *65*, 846–849. [[CrossRef](#)]
37. Islam, S.; Afefy, H.M.; Sennah, K.; Azimi, H. Bond characteristics of straight and headed-end, ribbed-surface, GFRP bars embedded in high-strength concrete. *Constr. Build. Mater.* **2015**, *83*, 283–298. [[CrossRef](#)]
38. Chen, S.M.; Li, H.H. Bond of Reinforcement in Ultra-High-Performance Concrete. Paper by Jiqiu Yuan and Benjamin Graybeal. *ACI Struct. J.* **2016**, *113*, 1130–1131.
39. Ji, X.-D.; Cong, X.; Dai, X.-Q.; Zhang, A.; Chen, L.-H. Studying the mechanical properties of the soil-root interface using the pullout test method. *J. Mt. Sci.* **2018**, *15*, 882–893. [[CrossRef](#)]
40. Maranan, G.; Manalo, A.; Karunasena, W.; Benmokrane, B. Pullout behaviour of GFRP bars with anchor head in geopolymer concrete. *Compos. Struct.* **2015**, *132*, 1113–1121. [[CrossRef](#)]
41. Kim, M.K.; Kim, D.J.; Chung, Y.S.; Choi, E. Direct tensile behavior of shape-memory-alloy fiber-reinforced cement composites. *Constr. Build. Mater.* **2016**, *102*, 462–470. [[CrossRef](#)]
42. Harajli, M.H. Bond Stress–Slip Model for Steel Bars in Unconfined or Steel, FRC, or FRP Confined Concrete under Cyclic Loading. *J. Struct. Eng.* **2009**, *135*, 509–518. [[CrossRef](#)]
43. Ho, H.V.; Choi, E.; Park, S.J. Investigating stress distribution of crimped SMA fibers during pullout behavior using experimental testing and a finite element model. *Compos. Struct.* **2021**, *272*, 114254. [[CrossRef](#)]
44. Abdallah, S.; Fan, M.; Cashell, K.A. Pull-out behaviour of straight and hooked-end steel fibres under elevated temperatures. *Cem. Concr. Res.* **2017**, *95*, 132–140. [[CrossRef](#)]

45. Dehghani, A.; Aslani, F. Effect of 3D, 4D, and 5D hooked-end type and loading rate on the pull-out performance of shape memory alloy fibres embedded in cementitious composites. *Constr. Build. Mater.* **2021**, *273*, 121742. [[CrossRef](#)]
46. Choi, E.; Mohammadzadeh, B.; Hwang, J.-H.; Kim, W.J. Pullout behavior of superelastic SMA fibers with various end-shapes embedded in cement mortar. *Constr. Build. Mater.* **2018**, *167*, 605–616. [[CrossRef](#)]

**Disclaimer/Publisher's Note:** The statements, opinions and data contained in all publications are solely those of the individual author(s) and contributor(s) and not of MDPI and/or the editor(s). MDPI and/or the editor(s) disclaim responsibility for any injury to people or property resulting from any ideas, methods, instructions or products referred to in the content.